

pubs.acs.org/JPCC Article

Structure-Controlled Chemical Properties of PdZn Near-Surface Alloys

Published as part of The Journal of Physical Chemistry virtual special issue "Cynthia Friend Festschrift".

Cory A. Milligan, Ranga Rohit Seemakurthi, Junxian Gao, Jeffrey P. Greeley, Jeffrey T. Miller, Fabio H. Ribeiro, and Dmitry Y. Zemlyanov*



Cite This: J. Phys. Chem. C 2022, 126, 13660-13674



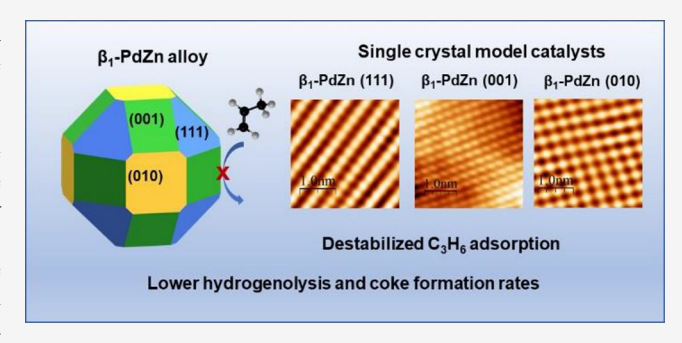
ACCESS

III Metrics & More

Article Recommendations

s Supporting Information

ABSTRACT: PdZn catalysts have demonstrated high potential in methanol steam reforming, water—gas shift reaction, and propane dehydrogenation. In order to understand the reaction mechanisms, β_1 -PdZn surface alloys were produced on Pd(111) and Pd(100) single crystal substrates via vapor deposition of diethylzinc. The structural properties and thermal stability of the surface alloys were investigated by X-ray photoelectron spectroscopy, low-energy electron diffraction, and scanning tunneling microscopy (STM) techniques. Several phases of the PdZn alloy were observed on the Pd(111) surface depending on the preparation conditions. On Pd(111), atomically resolved STM images show a transition from a PdZn p(2 × 1) rowlike structure to the β_1 -PdZn(111) surface to a



zigzaglike structure when annealed at increasingly higher temperatures. Similarly, a transition from the β_1 -PdZn(001) to the β_1 -PdZn(010) structure was observed when PdZn alloys were prepared on a Pd(100) single crystal. The adsorption of carbon monoxide and propylene was investigated by high-resolution electron energy loss spectroscopy. CO was found to bind exclusively in the linear position (no bridge configuration) for the β_1 -PdZn(010) surface, while complete destabilization of CO was observed on all other β_1 alloy surfaces. Propylene was found to no longer adsorb on any of the β_1 alloy surfaces even at subambient temperatures, 130 K. To complement the experimental observation, DFT calculations have been performed, which point to lower binding energies of CO and propylene on PdZn surfaces compared to Pd surfaces. This fundamental surface science study depicts the inability of propylene to adsorb on the 1:1 alloy terrace surfaces, thereby leading to the inhibition of deeper dehydrogenation, hydrogenolysis, and coke formation. Hence, this can be considered as one of the major factors for the high alkene selectivity and stability of PdZn alloy catalysts for alkane dehydrogenation.

1. INTRODUCTION

The PdZn alloy was first reported for its catalytic application for methanol steam reforming, where it was found that Pd on ZnO had a 97% selectivity toward ${\rm CO_2}$ and ${\rm H_2}.^{1-3}$ It was later discovered that under reducing conditions hydrogen spills over from the Pd catalyst particles and reduces the ZnO support generating a PdZn alloy, which was responsible for this improved selectivity.^{4,5} The PdZn alloy formation and its effect on methanol steam reforming were investigated on a flat surface of Pd(111).^{6,7} The PdZn surface has also been studied for the water—gas shift and propane dehydrogenation (PDH) reactions.^{8–10}

Palladium on SiO_2 has been shown to be a poor PDH catalyst as it undergoes rapid deactivation and has poor selectivity toward propylene. However, by alloying palladium with zinc on SiO_2 , the catalytic performance is enhanced where the propylene selectivity increases to >98% at 15% conversion. As verified by synchrotron XRD, the synthesis

procedure under reducing conditions leads to the formation of β_1 -PdZn nanoparticles. Since hydrogenolysis has previously been shown to be a structure sensitive reaction (requiring ensemble sites of multiple Pd atoms in specific arrangement) and PDH has been shown to be a structure insensitive reaction (requiring a reaction site with only a single atom), $^{10-13}$ the high olefin selectivity has been attributed to geometric changes of the surface caused by alloying with zinc. As alloying occurs, the surface becomes populated by inactive zinc atoms, and the Pd–Pd bond distance increases from 2.80 to 2.93 Å. However, the most stable crystallographic surfaces for PdZn ((111),

Received: March 9, 2022 Revised: July 18, 2022 Published: August 5, 2022





(110), and (100)) still contain adjacent Pd atoms; ¹⁴ hence, the improved selectivity has been primarily attributed to the elongation of the Pd-Pd bond and the dilution of large Pd surface ensembles by Zn. In the case of PDH, the increasing of the Pd–Pd distance should hinder the π binding of propylene, the product of PDH, and therefore inhibits the C-C bond cleaving reactions, increasing the selectivity toward propylene on PdZn catalyst. However, making definite conclusions regarding electronic and geometric effects using nanoparticle catalysts is complicated owing to several factors. For this specific purpose of understanding the geometric and electronic differences between alloys and pure metals, single crystal surfaces are useful because the exact structure and electronic differences can be revealed through surface sensitive techniques. Hence, the major focus of this study is to use well-defined single crystal surfaces of an alloy and the pure metal and compare their catalytic activities by using control experiments like adsorption of propylene and CO.

In order to simplify the complicity of the technical catalysts, in this study several intermetallic Pd-Zn surfaces were synthesized by ultrahigh vacuum-chemical vapor deposition (UHV-CVD) of Zn precursor onto Pd(111) and Pd(100). The relevant chemical and structural information on these surfaces was studied through multiple surface sensitive structural techniques, including scanning tunneling microscopy (STM) and low-energy electron diffraction (LEED), while the chemical information was obtained using surface sensitive chemical methods, including high-resolution electron energy loss spectroscopy (HREELS) and X-ray photoelectron spectroscopy (XPS). Adsorption properties of the PdZn surfaces toward carbon monoxide and propylene were investigated to understand the implications toward the reactivity of these catalysts for the propane dehydrogenation reaction. Furthermore, density functional theory studies were used to corroborate with experimental observations.

It should be noted that the PdZn alloy system has received ample attention from the surface science research community motivated by its importance for catalysis. Historically, Bayer et al. have grown the PdZn surface alloys by deposition of Zn on a Pd(111) surface followed by annealing. 15 They confirmed the PdZn(1:1) alloy by the observed (2×2) LEED pattern assigned to an ordered $p(2 \times 1)$ surface alloy structure and by XPS. It was demonstrated that the density of state (DOS) of the PdZn alloy surface and of the Cu(111) surface is very similar. 14-16 This was used to explain the similar catalytic activity of both systems in methanol steam reforming. The reduction of the population of the Pd 4d states in the near Fermi level region was consistent with previously reported catalytic results. 17,18 Weirum et al. have shown the STM results for the PdZn structure on the Pd(111) surface demonstrating that the observed (2×2) LEED pattern indeed represents three domains of the p(2 \times 1) structure. ^{19,20}

Rameshan et al. reported that the selectivity of methanol steam on the PdZn surface alloys is governed by the subsurface layers. A multilayer PdZn 1:1 near-surface alloy exhibits high CO₂ selectivity, whereas the monolayer PdZn 1:1 surface only produces CO and H₂, despite identical surface Pd/Zn ratios. Also, on the multilayer PdZn 1:1 near-surface alloy, CO was found to adsorb in the linear configuration, and the monolayer PdZn surface of the bridge CO_{ads} was detected by PM-IRAS spectroscopy. A similar adsorption trend was noted by Jeroro et al. for the Zn/Pd(111) alloy surfaces by HREELS, when the preferred adsorption sites for CO changed from threefold

hollow to atop sites with the zinc concentration increasing.²¹ Similar behavior was observed for supported Pd-Zn/Al₂O₃ catalysts, and the conclusion was that both ensemble and electronic effects play a role in how Zn alters the interactions of CO with the surface. The temperature-induced compositional and structural changes of the PdZn surface alloys on Pd(111) were investigated in the wide temperature range of 300-850 K.6,22 Above 550 K, quick Zn diffusion into the Pd bulk was observed, triggering the switching from the original Zn-out/Pd-in surface corrugation to Pd-out/Zn-in. This altered corrugation pattern was also detected when submonolayer amounts of Zn were heated to approximately 500 K. Despite the high quality of the discussed above publications, the structures of the PdZn surface alloys were not investigated at the full scale, and it is difficult to draw a conclusion about the adsorption site of CO.

CO adsorption also was used to probe the chemical properties of the bimetallic surface alloys such as PdAu, 23-27 PtAu, ²⁸ and PdAg, ^{29,30} which could be considered as similar to the PdZn surface alloys, in terms of the correlation between Pd surface concentration and CO adsorption sites. CO stretching at 2088 cm⁻¹ associated with CO adsorption on isolated Pd sites was reported in ref 25. Based on the frequency of the CO stretching mode, Wei et al.²⁵ concluded that the CO adsorption is mainly influenced by an ensemble effect without any significant contribution from a ligand effect. The surface concentration of isolated Pd sites was controlled by annealing Pd-Au alloy, and no long-range ordered structures were reported.^{23–27} On PdAg bimetallic surfaces, CO was adsorbed on Pd surface atoms and the Pd assembly sites, and similar to PdAu, the CO adsorption behavior was dominated by geometric ensemble effects.²⁹ The adsorption on the threefold hollow Pd sites was more stable than on the Pd bridge sites and finally the Pd on-top sites. 29,30

One of the conclusions we can make from the published PdZn data is that the surface composition and structure of the PdZn surface alloys somehow depend on the (i) Zn deposition amount and (ii) annealing temperature. The correlations between these two parameters and CO adsorption were reported. However, we have not found a publication that (i) clearly addresses the structures of the PdZn alloy surfaces formed under different conditions (the actually deposited Zn amount, annealing temperature, etc.) and (ii) clearly discusses the adsorption properties of them. Therefore, in this study we have tried to bridge this gap, and we have focused on the control of the surface composition and structure and have linked these parameters to the adsorption properties of carbon monoxide and propylene. Varying the symmetry of the PdZn structures allows us to distinguish better between "ensemble" and "ligand" effects, which are widely used to explain the origin of the enhanced activity or selectivity of bimetallic catalysts.

2. METHODS AND MATERIALS

2.1. Experimental Section. Experiments were performed in an Omicron Surface Analysis Cluster at the Birck Nanotechnology Center at Purdue University. The Omicron Cluster consists of a preparation chamber and a μ -metal analysis chamber with base pressures of 1×10^{-9} and 5×10^{-11} mbar, respectively. The preparation chamber contains Ar^+ sputtering, resistive sample heating, and leak valves for gas or metalorganic precursor dosing from gas manifolds. The analysis chamber is equipped with XPS, HREELS, STM, LEED, and resistive sample heating. In both chambers the

temperature of the sample is measured by k-type thermocouples connected to the sample holder. A Pd(111) and Pd(100) single crystal with 9.0 mm diameter and 1.0 mm thickness (MaTecK) with an orientation accuracy of <0.5° was used. The single crystals were cleaned by repeated cycles of Ar $^+$ sputtering and annealing in vacuum at 1000 K and in oxygen at 623 K. The cleanliness of the sample was monitored by XPS, LEED, HREELS, and STM.

Zn was deposited on the single crystals by vapor deposition using diethylzinc as the precursor (≥52 wt % Zn basis, Sigma-Aldrich). The preparation chamber was conditioned for deposition by exposing the chamber to diethylzinc (DEZ) at pressures of 1×10^{-7} mbar for 10 min, prior to transferring in the single crystal. During deposition the Pd(111) sample temperature was held between 300 and 750 K, while the DEZ, at room temperature, was exposed through a leak valve. An exposure of 450 L was used for surface temperatures between 300 and 473 K (1 L (Langmuir) = 10^{-6} mbar \times s), and an exposure of 2500 L was used for all higher temperatures. The increase in exposure was required to keep the quantity of Zn deposited on the surface relatively constant (3-5 ML equivalent) owing to the increasing mobility of zinc into the palladium bulk at elevated temperatures. In our study of zinc oxide ultrathin films on the Pd(111) surface, to deposit Zn we have used chemical vapor deposition (CVD) with DEZ and physical vapor deposition (PVD).³¹ No difference was detected for these two approaches. One of the advantages of CVD is that this approach requires only a leak-valve and a small stainless-steel cylinder (5–100 cm³), which can be easily transferred to another experimental rig. On the other hand, typically PVD requires to control reliably the amount of a deposited material by a quartz balance, which might give misleading readings especially for "nonvacuum" materials such as zinc. In our experiments, either CVD or PVD was used, and the amount deposited was always controlled by XPS.

HREELS data were acquired with an ELS5000 (LK Technologies). Electrons were collected in the specular direction with primary beam energies of 5 eV. The fwhm of the elastic peak was between 2.5 and 3.0 meV (20–24 cm⁻¹), and the elastic peak intensity was above 10⁵ cps for all spectra reported. All HREELS spectra have been normalized to the elastic peak intensity.

LEED patterns were acquired using an Omicron rear-view LEED optics with primary electron energies between 30 and 170 eV.

XPS data were collected using nonmonochromatic Mg K α X-rays (1253.6 eV) at an X-ray gun power of 150 W. High-resolution core level spectra were obtained at constant pass energy of 20 eV with an energy spacing of 0.05 eV. Electrons were collected at a 45° photoemission angle with respect to the surface normal. No energy scale correction was foreseen by the analyzer manufacturer (the electron energy analyzer–Omicron EAC 125 and the analyzer controller–Omicron EAC 2000); therefore, it was possible only to set the Pd 3d_{5/2} peak, of clean Pd(111), at 335.0 eV by changing the spectrometer work function. XPS data were analyzed using CasaXPS software. A typical error in determining the binding energy was <±0.1 eV; however, the peak position obtained through the curve fitting could deviate \pm 0.2 eV.

The procedure to calculate film thickness using XPS data is described in detail elsewhere,^{32–35} and brief details are provided in the Supporting Information. The thickness calculation procedure was adopted from ref 36, giving the

ratio between the photoemission peaks of a substrate and an overlayer. The practical electron attenuation length (EAL) (used instead of the inelastic mean free path) was calculated by NIST 82. The parameters are provided in the Supporting Information. To simplify the analysis, we assume that in all cases the PdZn(1:1) alloy forms an overlayer on Pd single crystal surfaces. This assumption does not always hold true, for instance in the case of a complex overlayer such as Zn/PdZn/Pd. Zn $2p_{3/2}$ or the PdZn component of the Pd 3d peaks can be chosen as the descriptor of the PdZn overlayer. The results of both calculations are given in Table 1.

Table 1. Thickness of the PdZn Alloys on Pd(111) and Pd(100) Surfaces^a

| preparation conditions | structure | thickness based on the intensity ratio of Pd 3d and Zn $2p_{3/2}$, Å | thickness based on the curve fitting of Pd 3d, Å |
|--|---|---|---|
| | On the Pd(| 111) Surface | |
| adsorption of DEZ at 300 K | no well-ordered structure | 7.3 | 2.6 |
| adsorption of DEZ at 373 K | $p(2 \times 1)$ | 14.1 | 10.2 |
| adsorption of DEZ at 473 K | β_1 -PdZn(111) | 25.6 | 25.2 |
| adsorption of DEZ at 473 K and annealing at 500 K | zigzag | 9.0 | 11.6 |
| | On the Pd(| 100) Surface | |
| adsorption of DEZ at 373 K | $eta_{	ext{1}}	ext{-PdZn(001)} \ 	ext{Zn-terminated}$ | 14.0 | 7.9 |
| adsorption of DEZ at 500 K | β_1 -PdZn(010) | 5.9 | 6.7 |

^aThe thickness was calculated either using the intensity ratio of Pd 3d and Zn $2p_{3/2}$ peaks or using the ratio between Pd metal and PdZn alloy components obtained by the curve fitting of the Pd 3d peaks. The details and parameters are in the Supporting Information and in the Experimental Section.

STM images were collected with an Omicron ambient temperature UHV STM/AFM. W tips were made via electrochemical etching followed by electron bombardment in UHV. Images were collected using a constant current scanning (topographic) mode. The bias varied between +0.5 and +1.0 V with tunnel currents ranging from +0.5 to +1.0 nA. In all experiments reported here, the tip was electrically grounded. The typical spatial resolution of STM is approximately 10% in the *x*- and *y*-directions and approximately 1% in the *z*-direction. The STM images were analyzed using WSxM software.³⁸

2.2. Density Functional Theory. The Vienna Ab initio Simulation Package (VASP) was used for all the periodic density functional theory (DFT) calculations performed in this study. The Kohn–Sham equations were solved self-consistently using the Perdew, Burke, and Ernzerhof (PBE) functional, with the projected augmented wave (PAW) method. The converged lattice constants for fcc Pd and tetragonal β_1 -PdZn were a=3.94 Å and a=2.9 Å, c=3.42 Å, respectively. For simulating the (111) and (100) facets of Pd, 3 × 3 × 5 and 4 × 3 × 5 unit cells were chosen, respectively. On the other hand, for simulating the (111) and (010) facets of PdZn, a 2 × 3 × 5 unit cell has been chosen. Finally, a 4 × 3 × 5 unit cell has been chosen to simulate the (001) facet of PdZn. The size of the unit cells was chosen to replicate the low

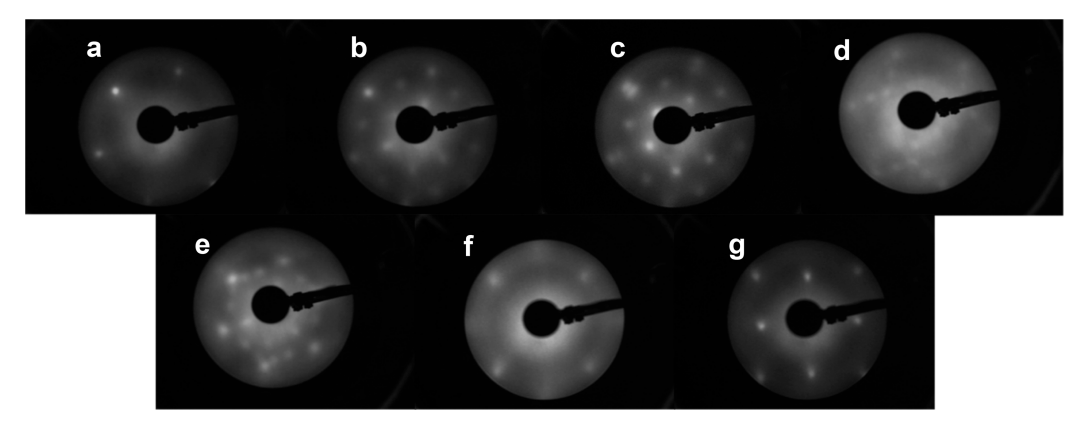


Figure 1. LEED patterns of diethylzinc deposited on (a) Pd(111) at room temperature (electron energy = 142 eV), (b) Pd(111) at 373 K (135 eV), (c) Pd(111) at 473 K (133 eV), (d, e) Pd(111) at 500 K following by annealing at 573 K (95 and 62 eV), (f) Pd(100) at 373 K (119 eV), and (g) Pd(100) at 473 K (99 eV).

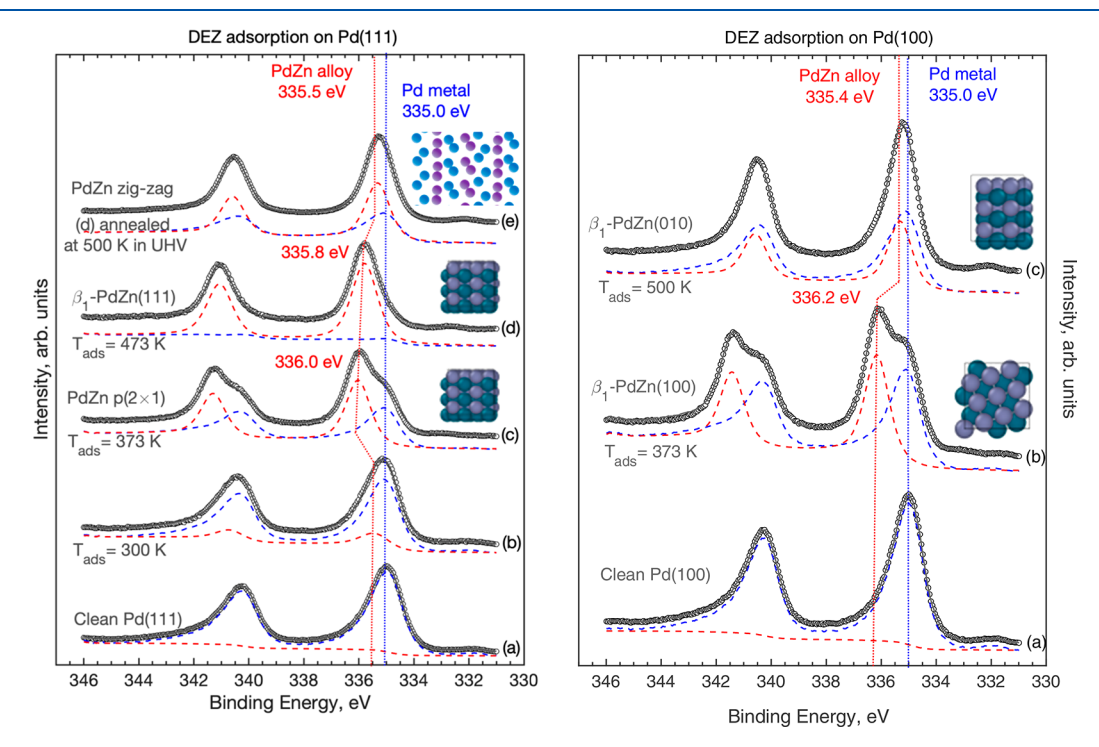


Figure 2. Pd 3d XPS spectra obtained following diethylzinc adsorption on Pd(111) (left panel) at RT (b), at 373 K, $p(2 \times 1)$ structure (c), at 473 K, β_1 -PdZn(111) structure (d), and following annealing of (d) in UHV at 500 K, zigzag structure (e) and on Pd(100) (right panel) at 373 K, β_1 -PdZn(001) Zn-terminated structure (b) and at 500 K, β_1 -PdZn(010) structure (c). Spectra (a) in both panels are from clean Pd single crystal surfaces. The Pd metal components are in blue, and the PdZn alloy components are in red. The structural assignment on the left of each spectrum was made in conjunction with STM and LEED data. The cartoon representations of the PdZn alloy structures are shown: blue, Pd; purple, Zn.

coverages of propylene adsorption on various facets. For the adsorption calculations, the DFT geometry optimizations were performed until the forces were converged within 0.02 eV/Ų. Furthermore, all the surface calculations have been performed using a plane wave energy cutoff of 400 eV with a 3 × 3 × 1 Monkhorst–Pack k-point grid and a vacuum of 15 Å in the z-direction. These values were confirmed to converge the adsorption energy calculations within 0.05 eV. All calculations were nonspin-polarized, and dipole corrections were applied in the z-direction to cancel out the net dipole moment on the slab. Finally, to determine the partial electron occupancies, the Methfessel—Paxton scheme was used with an energy smearing of 0.2 eV. The binding energies were estimated by subtracting the clean slab energy and the closed-shell gas phase species energy from the adsorbed configuration energy. The vdW

corrections were not included in this study, which will have an effect on the absolute values of binding energies. However, it was assumed here that the differences in binding energies across facets should be similar even after the inclusion of dispersion corrections. This has been discussed in greater detail in our previous study on the microkinetic analysis of propane dehydrogenation on the PdIn alloy surface.³⁹

3. RESULTS AND DISCUSSION

3.1. PdZn Alloy Structure. *3.1.1. Pd(111)*. The interaction of diethylzinc (DEZ) with Pd(111) was investigated by LEED (Figure 1), XPS (Figures 2 and 3), HREELS (the spectra are not shown here), and STM (Figure 4). The quantifications of the XPS data are summarized in Table 1. Four hundred fifty Langmuirs of DEZ was exposed to a freshly

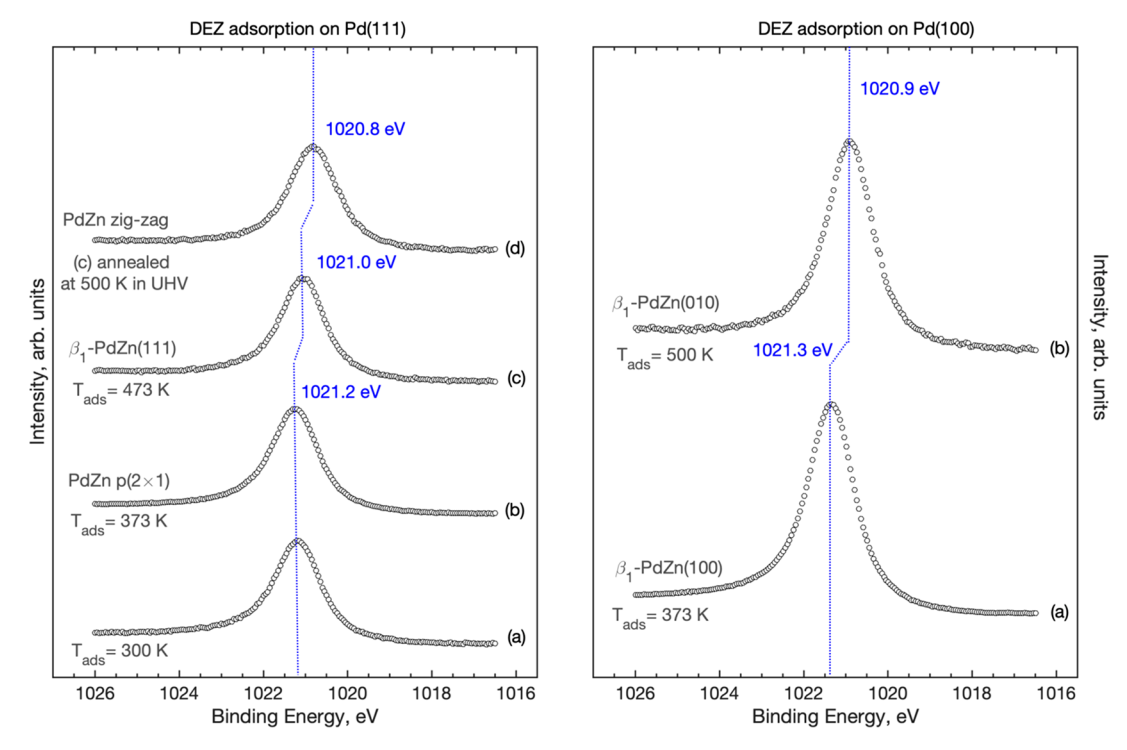


Figure 3. Zn $2p_{3/2}$ XPS spectra obtained following diethylzinc adsorption on Pd(111) (left panel) at RT (a), at 373 K p(2 × 1) structure (b), at 473 K, β_1 -PdZn(111) structure (c), and at 500 K, zigzag structure (d) and on Pd(100) (right panel) at 373 K, β_1 -PdZn(001) Zn-terminated structure (a) and at 500 K, β_1 -PdZn(010) structures (b). The structural assiment on the left of each spectrum was made in conjunction with STM and LEED data.

cleaned Pd(111) surface at room temperature (RT). DEZ adsorbs dissociatively under these conditions. Hydrocarbon fragments mainly desorbed, even at RT, as the carbon to zinc ratio measured by XPS was 1 to 6, well below the stoichiometric value of diethylzinc, which is 4 to 1. Weak HREELS peaks were observed following DEZ exposure at RT, which can be attributed to products of the C₂H₅ ligand (ethane and ethylene). No evidence of the formation of a PdZn alloy was observed at RT: XPS only shows a minimal shift in the Pd 3d binding energy (BE) from 335.0 to 335.1 eV (Figure 2), and the position of the Zn 2p_{3/2} peak corresponds to metallic zinc at 1021.2 eV (Figure 3), which is shifted by 0.5 eV with respect to the BE for bulk Zn. 40 Interestingly, the PdZn thickness calculated using the Zn 2p_{3/2} peak and the PdZn components is quite different and is equal to 7.3 and 2.6 Å (Table 1). The Zn 2p_{3/2} peak gives a much "thicker" PdZn overlayer, and we can conclude that this is just the failure of our simplified model, which is described as a simple PdZn overlayer on the Pd(111) surface. All XPS data, peak positions, and quantification consistently indicate that Zn forms a layer on top of Pd(111) or on top of ultrathin PdZn. As shown in Figure 1a, the LEED reflexes are weak and correspond to the (1×1) symmetry of the Pd(111) substrate. These results suggest that during DEZ adsorption/dissociation at RT, Zn film grows pseudomorphically on the surface of Pd(111). These results are consistent with the growth behavior observed using the more traditional PVD method with a metallic zinc source for growing PdZn alloys. 15,22

A slight increase of the adsorption temperature to 373 K during the DEZ exposure resulted in intermixing of zinc with palladium creating an ordered PdZn alloy. Two components of the Pd $3d_{5/2}$ XPS peak can be distinguished at 336.0 and 335.1 eV, corresponding to a PdZn intermetallic and pure Pd,

respectively (Figure 2).²² Zinc was characterized by a single Zn 2p_{3/2} peak shifted to 1021.3 eV (compared to the RT exposure) (Figure 3). The PdZn thickness also increased to 14.1-10.2 Å (Table 1). The relatively close number obtained for Zn 2p_{3/2} and for the PdZn intermetallic component also points to the intermixing of zinc with palladium. The increased amount of zinc compared to DEZ adsorption at RT could be explained by Zn inhibition of DEZ dissociation at lower temperatures. At elevated temperatures, zinc diffuses into the near-surface region of palladium releasing sites for DEZ dissociation. HREELS spectra of this surface, as well as all other surfaces prepared above 373 K, show no vibrational modes from residual hydrocarbon fragments from the DEZ molecule. The LEED pattern collected on this surface shows a well-defined $p(2 \times 1)$ structure of three rotationally symmetric domains (Figure 1b). This structure is commonly reported in the literature for PdZn surface alloys grown using PVD with a metallic zinc source. 41 As shown by STM (Figure 4a and 4b), this surface is characterized by alternating rows of Pd and Zn atoms, while maintaining the fcc-like structure of Pd(111), where the Pd-Pd distance is equal to 2.8 Å. It should be noted that STM probes the local density of states (LDOS) of the surface. Previous DFT calculations show that under the applied voltage conditions, the LDOS of palladium is significantly larger than zinc; thus, it is likely only the palladium atoms would be seen in STM. 42 On the other hand, Stadlmayr et. al provided detailed experimental evidence by impact-collision ion scattering spectroscopy (ICISS) and explained the alternating rows of the $p(2 \times 1)$ structure by lifting of the Zn atoms about 0.25 Å above the Pd atoms. 43 On the basis of only our STM data, we cannot say unambiguously that the bright rows are Zn atoms or Pd atoms. However, speculating on the STM contrast, we can suggest that the bright rows are

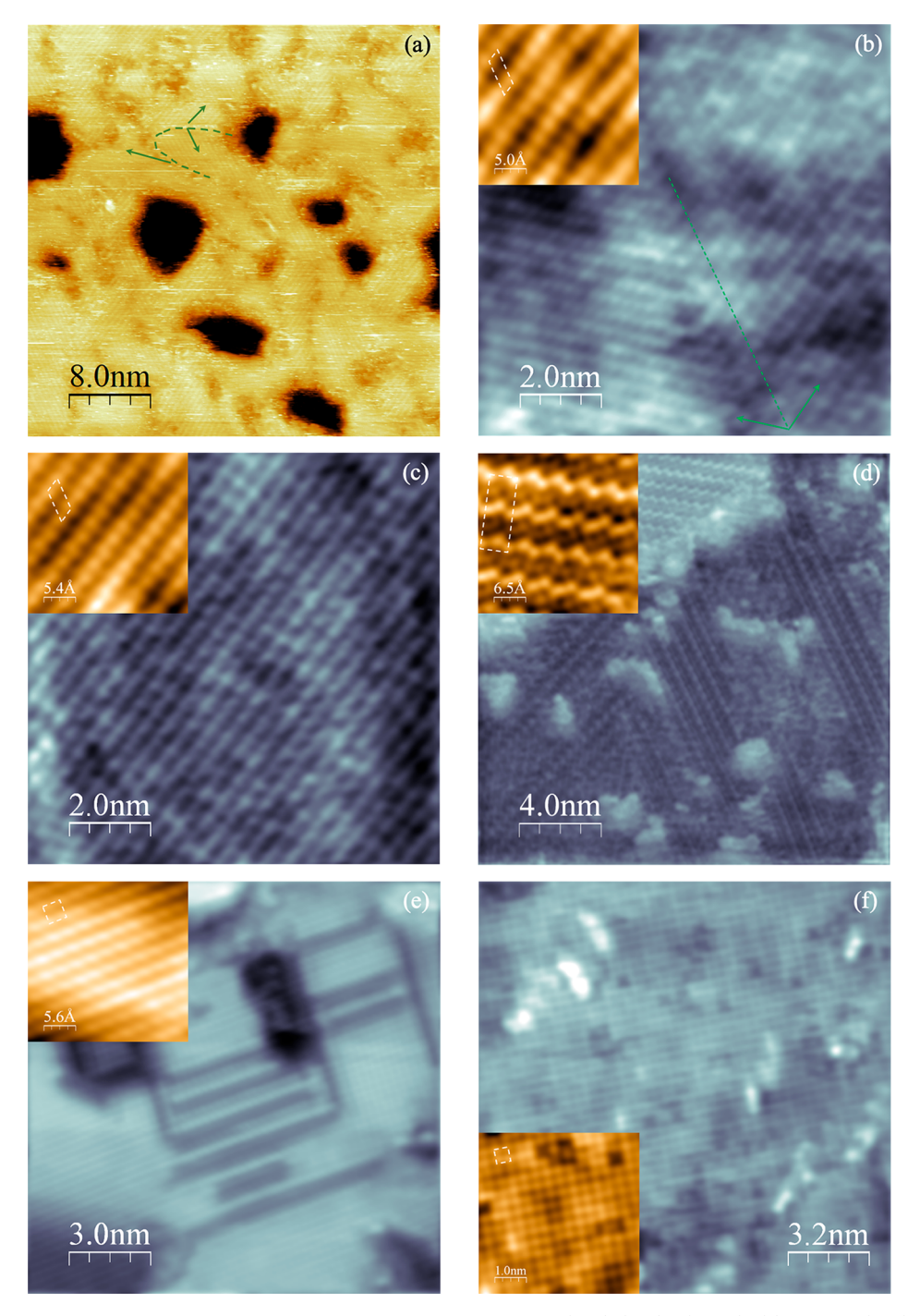


Figure 4. STM images of five structurally distinct PdZn surface alloys observed on Pd(111) (a, b) $p(2 \times 1)$, (c) β_1 -PdZn(111), and (d) zigzag and on Pd(100) (e) β_1 -PdZn(001) and (f) β_1 -PdZn (010). The synthesis conditions are as in Figures 2 and 3. The green dashed line and the green arrows in (a) and (b) are a guide for the eyes for a grain boundary between the $p(2 \times 1)$ domains and the dominant orientation, respectively. The white dashed tetragons in the insets are the proposed unit cell of the corresponding structures.

Pd rows. The p(2 \times 1) structure can be described by a parallelepiped unit cell of 2.8 \times 5.1 Å. The size of the p(2 \times 1) domains is 4–8 nm.

Following the DEZ exposure at 473 K, another surface structure is observed by LEED, as shown in Figure 1c. This LEED pattern, while qualitatively similar to the $p(2\times 1)$ structure, has some differences. The fractional reflexes became brighter. The doubling of the (1×1) reflexes appeared, and the doublet is shifted toward bigger k-space corresponding to a smaller lateral distance in real space. These changes would be

consistent with a transformation from the p(2 \times 1) fcc structure to the (111) surface of the tetragonal β_1 -PdZn alloy surface. While the atomic structures of both surfaces appear similar, the key difference is that the distance between adjacent Pd atoms on the surface has increased relative to the distance between adjacent Pd and Zn atoms. This β_1 -PdZn(111) surface is confirmed by STM, Figure 4c, where linear rows of atoms are observed with a parallelepiped unit cell of 2.7 \times 5.1 Å. XPS further supports the formation of the bimetal surface; thus, the Zn 2p_{3/2} peak is positioned at 1021.0 eV, slightly

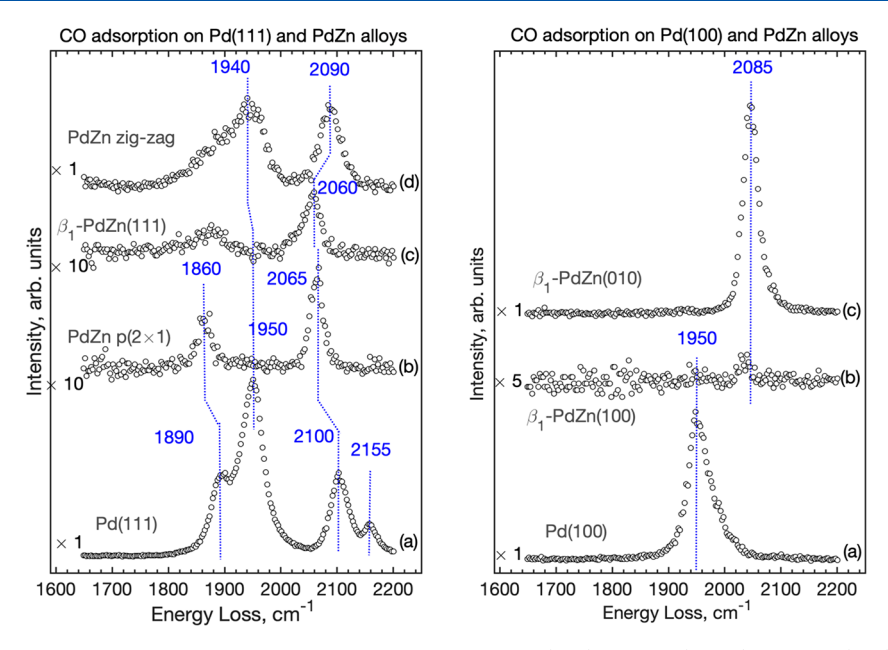


Figure 5. HREELS spectra following 5 L exposure of CO at 130 K. Left panel: Pd(111), PdZn p(2 × 1), β_1 -PdZn(111), and PdZn zigzag; right panel: Pd(100), β_1 -PdZn(001), and β_1 -PdZn(010). The intensities were normalized to an elastic peak. The coefficient of multiplication is on the left of each spectrum.

further toward lower BEs than in the previous case, and the Pd $3d_{5/2}$ peak now appears as a single broad symmetric peak positioned at 335.8 eV (Figure 2). The thickness of the PdZn overlayer is approximately 25 Å (Table 1). It is interesting that both calculations using Zn $2p_{3/2}$ or the Pd 3d component ratio give very close numbers pointing to good intermixing of Zn and Pd.

A complex LEED pattern was observed on the Pd(111) surface exposed to DEZ at 500 K followed by annealing at the temperatures of 523-573 K in UHV, as shown in Figure 1d and 1e. It should be noted that a lower kinetic energy of incident electrons (95 and 62 eV) is found compared to the previous LEED patterns (Figure 1a-c). This indicates a larger unit cell of the superlattice in the real space. Analyzing such a complex LEED pattern is difficult without the aid of dynamic LEED. This LEED pattern appears to be the same as the pattern reported by Gabasch et al. where it was assigned to a rectangular $(4\sqrt{3}/3 \times 6)$ superstructure.⁴¹ However, this identification becomes questionable when observed by STM. As shown in Figure 4d, the surface undergoes a complex restructuring into a zigzaglike structure; the cartoon representation is shown in Figure 2. This structure has quite large rectangular unit cell of 5.2 × 13.8 Å, and the proposed atomic arrangement is shown in the Supporting Information (Figure S2). Assuming Zn atoms show a lower contrast compared with Pd atoms, the surface Pd/Zn ratio is still 1:1. The Zn $2p_{3/2}$ peak again shifts toward lower BEs centered at 1020.8 eV. The Pd 3d_{5/2} peak consists of the contributions from the PdZn alloy at 335.5 eV and from reappearing metallic Pd at 335.0 eV. Therefore, the zigzag structure is likely also one of the forms of the β_1 -PdZn alloy with lower surface concentration of zinc owing to its diffusion into the bulk.^{6,22} The appearance of the metallic Pd at 335.0 eV points to the decrease of the PdZn alloy thickness down to 6-7 Å (Table

3.1.2. Pd(100). The preparation conditions for a Zn-modified Pd(100) surface were conducted much the same as for the Zn-modified Pd(111) surface. Four hundred fifty

Langmuirs of DEZ was exposed to a freshly cleaned Pd(100) surface held at a temperature of 373 K. No carbon is on the surface according to XPS (should be less than 0.5 at. %), and no evidence of hydrocarbon fragments from the DEZ precursor is seen by HREELS. XPS shows the Zn $2p_{3/2}$ peak located at 1021.3 eV (Figure 3), and the Pd 3d_{5/2} peak consists of two components at 335.1 and 336.2 eV; both Zn and Pd peak positions point to PdZn alloy formation (Figure 2).²² LEED carried out on this surface shows a symmetry identical with the unmodified Pd(100) substrate, (1×1) (Figure 1f). These results are consistent with the STM-detected square unit cell of 2.8×2.8 Å (Figure 4e). This lattice parameter is exactly equal to the Pd-Pd distance on the Pd(100) surface. This surface could be identified as a Zn- or Pd-terminated β_1 -PdZn(001) surface. On the other hand, the thickness of the PdZn overlayer was equal to 14.0 and 7.9 Å if the Zn 2p_{3/2}/Pd 3d (metal) ratio or the Pd 3d component ratio was used correspondingly. The former approach gives a higher number most likely owing to zinc enrichment on the surface. Therefore, we can suppose that the surface is Zn-terminated or even covered by a zinc layer. This conclusion is indirectly supported by CO adsorption as discussed below and by a low STM contrast. The Zn-terminated β_1 -PdZn(001) surface might have formed because of the kinetic limitations: the Zn atom accumulates on the surface rather than diffusing to the bulk at this temperature.

Increasing the exposure temperature to 500 K leads to a restructuring of the PdZn surface. Zinc is observed on the surface with a Zn $2p_{3/2}$ peak position of 1020.9 eV, a shift of 0.4 eV from the value for the β_1 -PdZn(001) surface. The Pd $3d_{5/2}$ peak is also seen to shift to a position of 335.2 eV and can be deconvoluted to the metallic Pd component at 335.0 eV and the alloy component at 335.4 eV (Figure 2). The PdZn alloy thickness is approximately 6 Å (Table 1). STM shows the formation of a well-ordered alloy with a rectangular unit cell of 3.8×3.4 Å (Figure 4e and 4f). The local density of states (DOS) in the vicinity of Pd atoms is higher than the DOS around Zn atoms; therefore, the observed atomic corrugation

might be assigned to the Pd atoms, and 3.9 and 3.4 Å correspond to the Pd–Pd distances. On the basis of the Pd/Zn atomic ratio and the periodicity of the surface, it is concluded that the (010) surface of the tetragonal β_1 -PdZn unit cell is formed.

Summarizing, in total five different structurally distinct PdZn surfaces were synthesized by this UHV-CVD preparation method on Pd(111) and Pd(100) surfaces, and the characterization was performed by LEED, XPS, HREELS, and STM techniques. Three of these surface structures could be directly linked to low index surfaces of the β_1 -PdZn crystal structure, i.e., β_1 -PdZn(111), β_1 -PdZn(001), and β_1 -PdZn (010).

3.2. Carbon Monoxide Adsorption. The preferred adsorption site of CO changes from bridge to linear when Pd alloys with Zn. 9,21 In addition, CO adsorption sites are sensitive to the Zn surface concentration. 21,22 Therefore, we used a carbon monoxide molecule as a probe for testing the adsorption properties of the PdZn alloys. Five PdZn surface structures described in the previous section were investigated as to CO adsorption following 5 L exposure at 130 K. Figure 5 shows the HREELS spectra of the stretching CO vibration region for CO_{ads} on the surfaces of the PdZn alloys synthesized on Pd(111) and Pd(100); the spectra of the CO adsorption on pure Pd(111) and Pd(100) are shown for comparison as well. CO adsorption on palladium surfaces was intensively studied in the past (see for instance refs 21 and 44-46 and references therein), and our observations are consistent with the literature. On the pure Pd(111) surface at 130 K, CO mainly adsorbs on threefold (the loss at 1890 cm⁻¹), bridge (1950 cm⁻¹), and on-top (or linear) (2100 cm⁻¹) sites; the highfrequency peak at 2155 cm⁻¹ can be attributed to adsorption on defect sites. 44 On the pure Pd(100) surface, CO only adsorbs on the bridge site with the CO stretching at 1950 cm^{-1} .

On the PdZn p(2 × 1) and β_1 -PdZn(111) surfaces, which were prepared at lower temperatures and, therefore, have higher Zn/Pd ratios, weak losses were detected at 2060-2065 and 1860 cm⁻¹ (as shown in Figure 5; the loss intensities are magnified by 10 times). The later losses could be either due to CO_{ads} on the threefold hollow sites or due to the bridge CO_{ads} with the stretching vibration shifted toward lower frequencies. The losses at 2060-2065 cm⁻¹ are assigned to the linear CO_{ads}; the peaks are also slightly shifted toward lower frequencies relative to the values on Pd(111). These lowfrequency shifts can be either (i) due to electronic modifications of the Pd atoms by the Zn atoms at high concentration or (ii) a result of weakening of the dipoledipole interaction at a low coverage. 45-47 The present data do not allow to distinguish between these two effects. Considering both the relative intensity and the lower frequency (if due to the dipole-dipole interaction), it is likely that any adsorbed carbon monoxide is present at very low local coverages even on defect sites of the PdZn surface. The low CO coverage could point to destabilization of the adsorption on Pd atoms owing to the electronic effect of the surrounding Zn atoms. This is different compared with CO adsorption on PdAu and PdAg surface alloys, when CO adsorption is dominated by geometric ensemble effects without any significant contribution from the electronic ligand effect. 25,29 It looks like Zn has a substantial electronic ligand effect on Pd. The PdZn "zigzag" phase was prepared by annealing of β_1 -PdZn(111) surfaces at 500 K, and therefore, zinc concentration was reduced owing to diffusion of zinc to the palladium bulk. As shown in Figure 5, CO adsorbs

in the bridge (1940 cm⁻¹), linear (2090 cm⁻¹), and threefold hollow (low-frequency shoulder of the peak at 2090 cm⁻¹) configurations. The PdZn zigzag structure shown in Figure 2 and in greater details in Figure S2 (Supporting Information) contains pairs of Pd atoms providing the bridge adsorption sites. The threefold adsorption is likely due to CO_{ads} on the Pd agglomerates-defects. It should be noted that judging from the peak intensities, the ratio between the linear and bridge CO_{ads} forms increases compared with pure Pd(111). Another observation pointing to the substantial electronic ligand effect of Zn on Pd is the relatively lower frequency of CO stretching vibrations, which is consistent with our DFT modeling (Table 3).

In the case of Pd(100), no CO adsorption was detected on the $\beta_1\text{-PdZn}(001)$ surface owing to the Zn termination (the spectrum was multiplied by five times). On the $\beta_1\text{-PdZn}(010)$ surface, the CO adsorption behavior changes drastically: the linear configuration (C–O stretching at 2085 cm $^{-1}$) is detected with the intensity close to those on the pure Pd(100) surface. This is quite remarkable because on palladium CO typically adsorbs in the bridge configuration. We supposed that this changing of the CO adsorption behavior is mainly due to geometric ensemble effects: the Pd–Pd distance is too big to form the bridge CO $_{\rm ads}$.

Our results of CO adsorption obtained on the model PdZn surfaces can help one to understand the results observed on supported nanoparticle catalysts. A nanoparticle has several majority faces including (111) and (100). As we demonstrate, Pd–Zn alloying might form different structures on Pd(111) and Pd(100). It is likely that the linearly adsorbed CO signal results from the adsorption on the PdZn(010) facets of the nanoparticle, which forms on the Pd(100) facets. The bridging and threefold hollow adsorption would be attributed to adsorption either on low coordination sites (edges or corners) similar to step edges on the planar surfaces or on zigzaglike structures enriched with Pd (Zn lean).

The strong destabilization of CO adsorption on the PdZn alloy surface was reported. The preferential adsorption of CO in the linear configuration was observed on the supported nanoparticle catalysts 9,21 and on Zn/Pd(111). However, we can suppose that the dominating effect on the CO adsorption depends on the PdZn structure. Thus, on the p(2 \times 1) surface the electronic ligand effect dominates, whereas on the β_1 -PdZn(010) surface the geometric ensemble is a major contributor as discussed below.

The lack of adsorption on either the β_1 -PdZn(111) surface or the $p(2 \times 1)$ surface is an intriguing result as both of these surfaces still contain exposed palladium atoms. A common rationality used to explain the increase in the relative amount of linear to bridge bound species is purely a structural phenomenon (geometric ensemble effect). Zinc will functionally dilute the palladium atoms on the surface (roughly speaking substituting every other Pd atom with Zn atom), destroying the larger ensembles required for multiply coordinated CO adsorption (bridge and threefold), while leaving linear bound adsorption sites. If the number of the adsorption sites for linear CO_{ads} indeed does not change due to Zn, the β_1 -PdZn(111) surface and the p(2 × 1) surface should still adsorb CO in the linear orientation with an intensity similar to that on pure Pd(111) at this temperature (assuming that the intensity is proportional to the coverage). Because the weak C-O stretching vibrations were detected, the low CO adsorption can be attributed, in some way, to a change in the

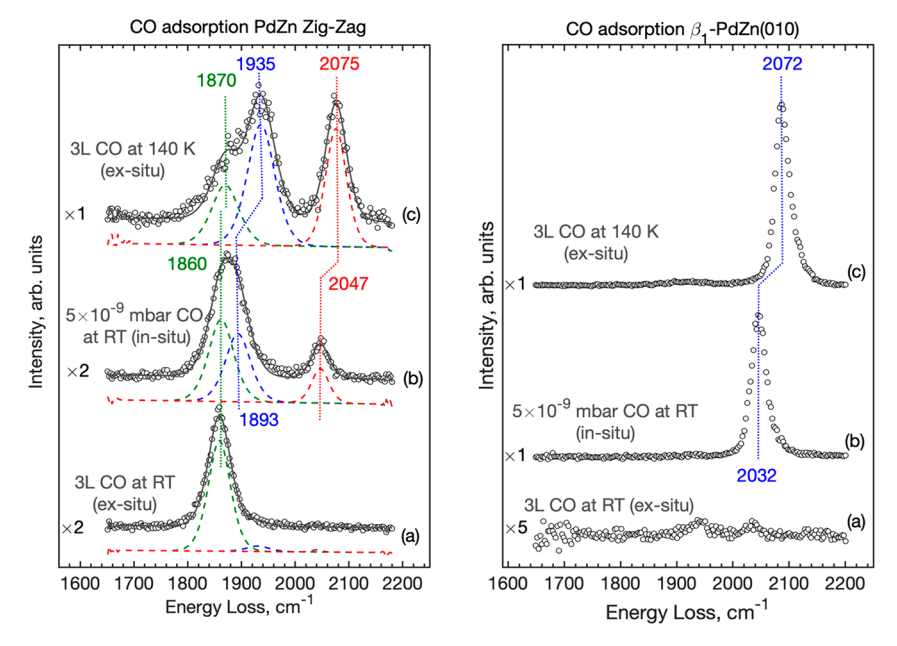


Figure 6. HREELS spectra of CO adsorption on the PdZn zigzag (left panel) and β_1 -PdZn(010) (right panel) surface after a series of CO exposure conditions. The three-hollow peaks are green, the bridge peaks are blue, and the on-top are red. The intensities were normalized to an elastic peak. The coefficient of multiplication is on the left of each spectrum.

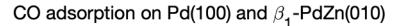
electronic properties of the surface palladium atoms due to zinc (electronic ligand effect). Analyzing CO adsorption on the $\beta_1\text{-PdZn}(010)$ surface, where only the on-top CO $_{\rm ads}$ was detected, we can conclude that the electronic ligand effect is strongly direction dependent: the p(2 \times 1) and $\beta_1\text{-PdZn}(010)$ surfaces have approximately equal Pd/Zn ratios, so the Pd atoms should be effected by the Zn atoms at the same magnitude. However, the symmetry of the structure controls the leading effect.

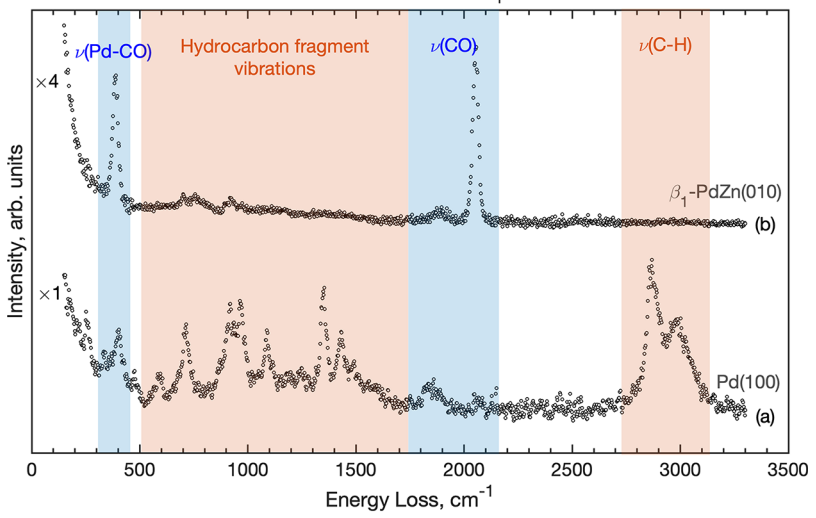
The zigzag and β_1 -PdZn(010) still allow for carbon monoxide adsorption. To further analyze the adsorption of CO on these intermetallic surfaces, these two PdZn surface structures were investigated under a variety of adsorption conditions. HREELS measurements were performed (a) ex situ at RT following a 3 L exposure, (b) in situ at RT at p(CO) = 5 \times 10⁻⁹ mbar, and (c) ex situ at 140 K following a 3 L exposure. As shown in Figure 6, no CO was detected ex situ following a 3 L exposure on the β_1 -PdZn(010) surface at 300 K. However, on pure Pd(100), CO is stable until 450 K;⁴⁹ this indicates a significant decrease in the adsorption energy of CO on the β_1 -PdZn(010) surface. However, the linear bound CO appears (the peak at 2032 cm⁻¹) on the surface during the in situ HREELS experiment as the background CO pressure is increased to 5×10^{-9} mbar, which is similar to the lowtemperature adsorption when at 140 K only linear bound CO_{ads} was detected ex situ as the CO stretching at 2072 cm⁻¹. The stretching frequency decreases between the ex situ lowtemperature experiment and the in situ 5×10^{-9} mbar experiment from 2072 to 2032 cm⁻¹, which suggests a low local surface CO coverage resulted in decreasing the dipoledipole interactions during the in situ experiment.

On the zigzag surface, the only stable adsorption is on the threefold hollow site, as shown by a single peak at 1860 cm⁻¹ at RT after a 3 L exposure (Figure 6). Likely, the zigzag PdZn structure provides plenty of the threefold sites, and CO adsorption on the threefold sites is significantly stronger than bridge and linear bound CO. A similar CO stability was reported on the PdAg alloy surfaces.^{29,30} Interestingly, judging

from the CO stretching intensity, the CO_{ads} on the threefold site does not experience strong destabilization by Zn most likely because the threefold sites are Pd agglomerates surrounded by the PdZn alloy. Upon increasing the base pressure of CO to 5×10^{-9} mbar, the bridging (1893 cm⁻¹) and linear bound (2047 cm⁻¹) CO_{ads} populate. Upon removal of gas phase CO, the HREELS spectra revert back to the one observed under UHV; i.e., only the threefold CO_{ads} was detected (as in Figure 6a, left panel). The significant decrease in the adsorption energy of CO indicates a significant electronic change in the surface Pd atoms. The lowtemperature CO adsorption on the PdZn zigzag surface at $140~\mathrm{K}$ demonstrates all three $\mathrm{CO}_{\mathrm{ads}}$ states: the threefold (1870 cm⁻¹), bridge (1935 cm⁻¹), and linear (2075 cm⁻¹) bound CO_{ads}. The intensity of the HREELS losses is not always directly proportional to the coverage. One of the main parameters affecting the HREELS intensity is the normal projection of a dynamic dipole moment of an adsorbate, which can be influenced by the electronic interaction between a substrate and an adsorbate. The dipole-dipole interaction between adsorbed species also results in the change of the HREELS intensity. On the other hand, the HREELS intensity can be used for quantification (see for instance ref 50). Therefore, under the assumption that the HREELS intensity is somehow proportional to the coverage, the similar intensities of the linear and bridge CO_{ads} stretches (Figure 5b-d) might indicate that the population of the linear CO_{ads} is comparable with the value for the bridge CO_{ads}. All HREELS peaks are shifted toward higher frequency pointing to the high local coverage (because of the higher dipole-dipole interaction).

3.3. Propylene Adsorption. The site isolation due to a longer distance between adjacent Pd atoms (Figure 4) of the intermetallic alloy surfaces could be a reason for the improved selectivity and Turnover Rate (TORs) of the PdZn catalyst for PDH, methanol reforming, water gas shift, etc. The poor stability and low propylene selectivity of monometallic Pd catalysts in PDH have been proposed to be due to further dehydrogenation and hydrogenolysis of strongly adsorbed





CO adsorption on Pd(111) and PdZn alloys

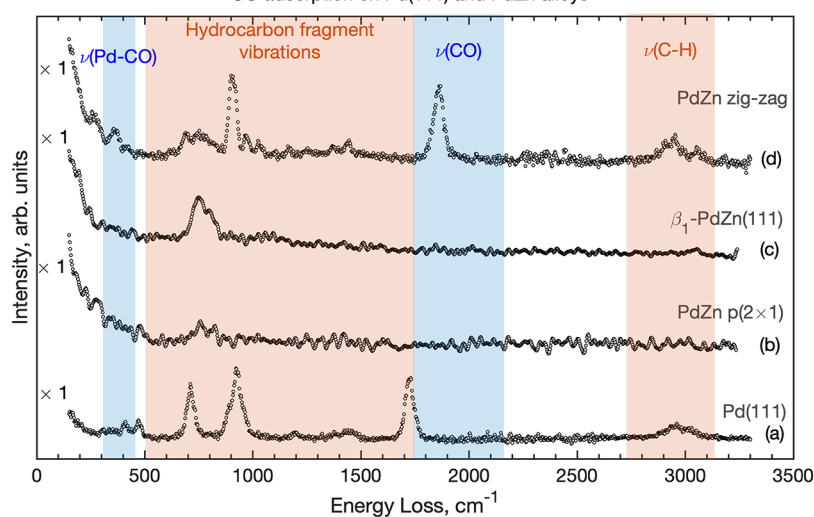


Figure 7. HREELS spectra following 5 L exposure of propylene at 130 K on Pd(111), PdZn p(2×1), β_1 -PdZn(111), PdZn zigzag, Pd(100), and β_1 -PdZn(010). Color marked regions are only for eye guidance: blue is for CO vibrations, and rose is for hydrocarbon vibrations.

propylene, which eventually also lead to coke formation on the surface. To test this hypothesis, propylene was adsorbed on Pd(111) and Pd(100) along with the PdZn model alloy surfaces at 140 K. The HREELS spectra are shown in Figure 7.

On both Pd(111) and Pd(100), propylene adsorbs in disigma-bounded fashion. Table 2 summarizes the main vibrational frequencies and the peak assignments. Propylene does not adsorb on the alloy surfaces except for the zigzag surface (Figure 7). The feature at 750 cm⁻¹ on the p(2 × 1) and β_1 -PdZn(111) surface is assigned to the phonon vibration of the PdZn alloy, while the peaks at 385 and 2055 cm⁻¹ on the β_1 -PdZn(010) surface are due to the CO adsorption from the UHV background. As listed in Table 2, the vibrational frequencies on the zigzag surface match well with the disigma-bounded propylene, which requires adjacent Pd atoms. Because on the zigzag surface CO adsorbs in threefold hollow and bridge sites, this surface provides plenty of adjacent Pd atoms.

These results indicate that the low-index surfaces of the PdZn alloy catalyst are unable to readsorb the propylene product potentially, leading to a more olefin selective catalyst

because these adsorbed surface species do not undergo further dehydrogenation and hydrogenolysis reactions. There is also an apparent correlation in the ability for a surface to adsorb multiply coordinated CO and their ability to adsorb propylene. This result indicates that CO adsorption could be used as a first pass screening of future catalyst compositions.

3.4. Density Functional Theory Results. To better understand the HREELS spectra of CO and propylene, adsorption calculations were performed using DFT on the ordered Pd and PdZn surfaces. Additionally, vibrational frequency analysis was done on the most stable adsorption configurations of CO and propylene. The (111) and (100) surfaces of the Pd, along with (111), (010), and (001) surfaces PdZn surfaces were simulated using the bulk fcc structure of Pd and the tetragonal structure of PdZn, respectively (Figure 8). The Pd—Pd distances in the relaxed PdZn(111) surface were 2.9 and 4.5 Å, while the distances in PdZn(010) were 3.4 and 4.1 Å. For the PdZn(001) Pd-terminated surface, the Pd—Pd distances were 2.9 and 2.9 Å, owing to its square symmetry. The same Zn—Zn distances were observed for the PdZn(001) Zn-terminated surface. Except for PdZn (001) surface, these

Table 2. Assignment of the Vibrational Frequencies Detected in the HREELS Spectra Following Propylene Adsorption on Pd(111), Pd(100), and PdZn Zigzag Surfaces and Comparison with the Literature Data^a

| assignment (adsorbed species) ^b | gas phase (IR) ^{14c} | C ₃ H ₆ on Pd(111) | C_3H_6 on $Pd(100)$ | C ₃ H ₆ on PdZn zigza |
|---|----------------------------------|--|-----------------------|--|
| C-CH $_3$ tr di- σ configuration | 193 ^a " | | 260 | 260 |
| | | 340 | 340 | 355 |
| C=C-C b | 426° | 410 | 400 | |
| | | 470 | 480 | |
| C-CH $_2$ tw di- σ configuration | 578ª" | | 590 | |
| | | 710 | 710 | 690 |
| | | | | 750 |
| $	ext{CH}_2$ w di- σ configuration | 908ª" | 885 | 885 | 900 |
| C-C st + CH ₂ r di- σ configuration | 916 ^{a'} | 925 | 920 | 920 |
| $CH_3 r + CH b + CH_2 r$ | $932^{a\prime}$ | | | |
| CH b + CH ₂ tw di- σ configuration | 988ª" | | 970 | 970 |
| CH ₃ r | 1040 ^a " | | 1035 | 1025 |
| | | | 1090 | |
| $CH_2 r + CH_3 r$ | 1169 ^a ′ | 1195 | 1200 | |
| CH b + CH ₂ b | 1293a' | | 1260 | |
| CH_3 s d + CH_2 sc di- σ configuration | 1370 ^a ′ | 1375 | 1350 | 1370 |
| CH ₂ sc + CH b + CH ₃ s d | 1411 ^a ′ | | | |
| CH ₃ as d | 1433a" | | | |
| CH_3 as $d + CH_2$ sc $di-\sigma$ configuration | 1449 ^a ′ | 1450 | 1430 | 1445 |
| Ü | | | 1490 | |
| $C=C st + CH_2 sc$ | 1645a' | 1725 | | |
| CO st d | | | 1850 | 1865 |
| CH ₃ s st di-σ configuration | 2912ª′ | 2895 | 2880 | 2910 |
| CH ₃ as st | 2933a" | | | |
| CH_3 as st + CH st di- σ configuration | 2958ª' | 2955 | | 2955 |
| CH_2 s st + CH st di- σ configuration | 2977 ^a ′ | | 2975 | 2970 |
| CH st di- σ configuration | 3008a' | 3025 | 3045 | 2990 |
| CH ₂ as st | 3075 ^{ca} | | | 3060 |
| a 4 11 C : | . 1 . | -1 <i>b</i> | 1 | 1 1. |

"All frequencies are reported in cm⁻¹. ^bas = asymmetric, b = bending, d = deformation, r = rock, s = symmetric, sc = scissors, st = stretch, tr = torsion, tw = twist, w = wag. ^cSymmetry a': in the molecule plane. Symmetry a": perpendicular to the molecule plane.

distances match within the error of experimentally observed bond distances in the STM images (the experimental error of STM in the lateral direction is approximately 10%).

3.4.1. CO Adsorption DFT Results. Table 3 shows the binding energies and vibrational frequencies corresponding to different adsorption sites on Pd and PdZn surfaces. CO is most stable in the hollow site (hcp) on Pd(111) with a binding energy of -2.02 eV, while the bridge and on-top configurations are less stable by 0.2 and 0.6 eV, respectively. On the Pd(100) surface, the adsorption of CO is most stable in the bridge configuration with a binding energy of -1.94 eV. In contrast to the strong adsorption on the Pd(111), the alloy surfaces of PdZn weakly adsorb CO. On β_1 -PdZn(111) CO adsorption is equally stable on on-top-Pd and bridge-Pd—Pd with a binding energy of -0.91 eV, which is 1.11 eV weaker compared to the

most stable site of Pd(111). This strong decrease in binding energies of CO on the β_1 -PdZn(111) surface in comparison to the Pd(111) surface leads to the disappearance of HREELS peaks on the alloy surface (Figure 5).

The binding energy of the linear CO_{ads} and the bridge CO_{ads} is -0.91 eV on the β_1 -PdZn(111) surface (corresponding to the zigzag surface in the experiment), and these numbers are -1.12 and -0.86 eV for the β_1 -PdZn(010) surface (Table 3). The CO adsorption is strongest on the β_1 -PdZn(010) surface, and the most stable site is now the on-top-Pd site, which is consistent with the experimental results (the right panels, Figure 5c and Figure 6c). The stronger adsorption of the linear CO_{ads} can be attributed to the longer Pd—Pd distances in the (010) surface (3.4 Å) than the (111) surface (2.9 Å). On the β_1 -PdZn(010) surface, the energy difference of 0.26 eV between the linear CO_{ads} and the bridge CO_{ads} is large enough to suppress the bridge CO_{ads} even at 130 K and in 5 × 10⁻⁹ mbar of CO at RT (Figure 6, right panel).

It is interesting to note that, on the β_1 -PdZn(111) surface, DFT predicts similar binding energies for linear and bridge CO_{ads} configurations. This is in agreement with experiments, where the linear and bridge CO_{ads} appear simultaneously in 5 \times 10⁻⁹ mbar of CO at RT and at 130 K (Figure 6, left panel). The good agreement between DFT and the HREELS data validates our modeling results, which predict the weakening of CO adsorption on the PdZn alloy surfaces and the population of CO_{ads} sites correctly.

For the β_1 -PdZn (001) surface, the Pd-terminated surface binds CO on the bridge Pd-Pd site with a binding energy of -1.49 eV, while the fourfold hollow site and on-top-Pd sites are unstable by 0.08 and 0.33 eV, respectively. The adsorption is far weaker on the PdZ (001) Zn-terminated surface with a binding energy of -0.4 eV on the on-top-Zn site. Because there were no CO peaks observed for the PdZn(001) surface, it is likely that the surface formed under experimental conditions is most likely a Zn-terminated surface. This conclusion can be explained as follows: among all the alloy surfaces considered, the PdZn(001) Pd-terminated had the highest CO binding energy, which is 0.37 eV greater than on the PdZn(010) surface, which showed a CO peak at 130 K. Hence, if the Pd-terminated PdZn(001) surface was formed under experimental conditions, we would except it to show a CO adsorption peak, which is not the case. Thus, it can be concluded that the PdZn(001) surface observed in experiments is a Zn-terminated surface. Finally, comparing the DFT predicted vibrational frequencies with the experiments, we observe that the errors are within 100 cm⁻¹ for the bridge and hollow sites, while the errors for the on-top sites are slightly lower (within 60 cm⁻¹). The errors can be attributed to both the intrinsic errors in the DFT calculations and the difference in coverages between experiments and the simulated low coverages.

3.4.2. Propylene Adsorption DFT Results. Similar to CO adsorption, propylene binding is weakened on the PdZn alloy surfaces compared to the pure Pd surfaces (Table 4). Propylene is most stable in the bridge or the di- σ configuration on both Pd(111) and Pd(100) surfaces. The binding energy is slightly stronger by 0.07 eV on the (100) surface as compared to the (111) surface. This strengthening is attributed to the smaller coordination number of Pd(100) surface atoms as compared to Pd(111). Conversely, on the β_1 -PdZn(111) surface, the most stable site is the on-top-Pd or the π configuration. The calculated propylene binding energy is

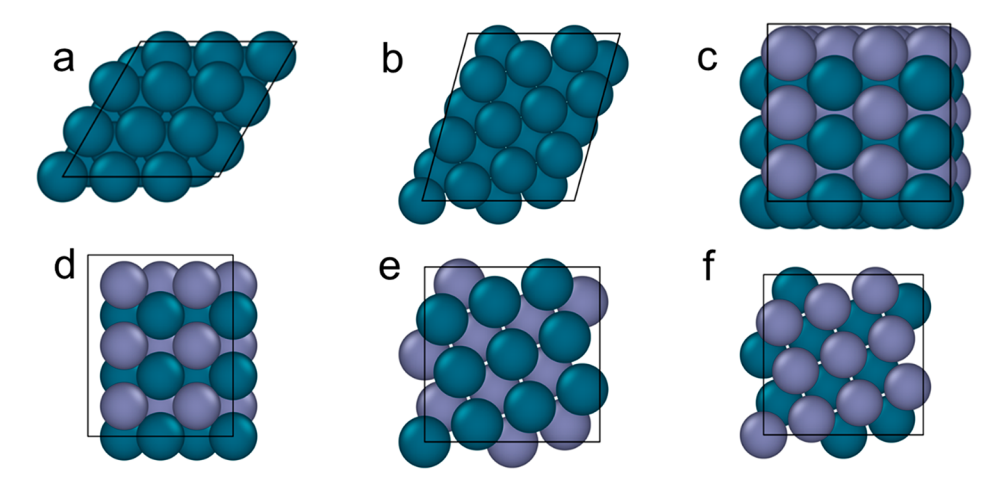


Figure 8. Surface slab models for (a) Pd(111), (b) Pd(100), (c) β_1 -PdZn(111), (d) β_1 -PdZn(010), (e) Pd-terminated β_1 -PdZn(001), and (f) Zn-terminated β_1 -PdZn(001). Blue, Pd; purple, Zn.

Table 3. Calculated C-O Stretching Frequencies and Binding Energies on Different Pd and PdZn Alloy Surfaces

| | Pd(111) | | | | PdZn(111) | | |
|---|------------------------------------|----------------------------|------------------------------------|---------------------|------------------------------------|-------------------------|--|
| CO _{ads} | site C–O stre | tching (cm ⁻¹) | binding energy (eV) | C–O stretchi | ng (cm ⁻¹) bin | ding energy (eV) | |
| on-to | p : | 2038 | -1.41 | 2019 | -0.91 | | |
| bridge | e ^a | 1851 | -1.82 | 187 | 7 | -0.91 | |
| hollov | W | 1773 | -2.02 | | | | |
| | Pd(10 | Pd(100) | | PdZn(010) | | PdZn(001)_Zn-terminated | |
| CO _{ads} site | C-O stretching (cm ⁻¹) | binding energy (eV) | C-O stretching (cm ⁻¹) | binding energy (eV) | C-O stretching (cm ⁻¹) | binding energy (eV) | |
| on-top | 2021 | -1.48 | 2017 | -1.12 | 1972 | -0.4 | |
| bridge ^b | 1855 | -1.94 | 1865 | -0.86 | | | |
| hollow | 1675 | -1.85 | | | | | |
| ^a Bridge-Pd-Pd for PdZn(111). ^b Bridge-Pd-Pd for PdZn(010). | | | | | | | |

Table 4. Calculated Propylene Binding and C-C Stretching Frequencies on Pd and PdZn Surfaces

| | Pd(111) | | | | PdZn(111) | | |
|------------------------|--------------------|--------------------------------|------------------------------------|---------------------|------------------------------------|---------------------|--|
| propylene s | ite C-C | stretching (cm ⁻¹) | binding energy (eV) | C–C stretchi | ng (cm ⁻¹) bin | ding energy (eV) | |
| bridge Pd- | Pd | 868, 1122 | -0.79 | 880, 1528 | | -0.13 | |
| on-top-Pd | | 867, 1483 | -0.66 | | | | |
| | Pd(100) | | PdZn(010) | | PdZn(001)_Zn-terminated | | |
| CO _{ads} site | C-C stretching (cm | binding energy (eV) | C-C stretching (cm ⁻¹) | binding energy (eV) | C-C stretching (cm ⁻¹) | binding energy (eV) | |
| bridge Pd–Pd | 868, 1148 | -0.86 | | | 1972 | -0.4 | |
| on-top-Pd | 885, 1479 | -0.77 | 873, 1522 | -0.41 | | | |
| physisorbed | | | | | -0.08 | | |

-0.13 eV, which is 0.66 eV weaker than on the Pd(111) surface. On the β_1 -PdZn (010) surface, the binding energy is -0.41 eV, and the most stable configuration is still the on-top-Pd site. Finally, on the Zn-terminated β_1 -PdZn (001) surface, the propylene adsorbs in a physisorbed state with a binding energy of -0.08 eV.

The vibrational frequency analysis shows that C-C stretching frequencies for bridge configurations on pure Pd(111) and (100) are 868 and 1130 cm⁻¹. This result is in line with the observed C-C peaks at around 920 and 1200 cm⁻¹ from the HREELS experiments. For the on-top configurations on both surfaces, the corresponding C-C stretch frequencies are around 870 and 1480 cm⁻¹. On the Pd(111) surface, there are no C-C stretch frequencies observed in experiments around 1480 cm⁻¹ (Table 2), indicating that most of the propylene adsorbed is in a disigma configuration. However, on Pd(100), HREELS experiments

show that there is a C-C stretch frequency of around 1490 cm⁻¹, which indicates that propylene may bind in both sigma and pi configurations on the (100) surface.

On PdZn surfaces, because propylene adsorbs only on the on-top-Pd site, the C-C stretching frequencies on the PdZn alloy surfaces are around 880 and 1520 cm⁻¹. However, as mentioned in the discussion of the HREELS experiments, there are no peaks observed in this range (800–1600 cm⁻¹) for the alloy surfaces except for the PdZn zigzagged surface. Hence, it can be concluded that the weak binding energies of propylene on the alloy surfaces do not allow for propylene adsorption, even at temperatures as low as 130 K. The low-temperature results can be roughly extrapolated to high-pressure experiments. Because propylene adsorption is suppressed on the PdZn terrace surfaces at 130 K, it will be inhibited at ambient pressure as well. Also, the low-binding energy of the propylene means a short resident time of the

molecule on the surface especially at the elevated temperatures of PDH reaction (\sim 800 K), thereby decreasing propylene propensity to undergo deep dehydrogenation and C–C bond breaking reactions. We propose that this difference in the binding ability of propylene is one of the reasons for higher propylene selectivity observed on the PdZn alloys compared to pure Pd. Further, the slight decrease in selectivity and the deactivation due to coke formation might be attributed to defects, for instance in the form of the zigzag phase, possibly appearing on the PdZn nanoparticles.

4. SUMMARY AND CONCLUSIONS

The adsorption of CO and propylene was compared on the clean palladium single crystal surfaces of Pd(111) and Pd(100) and on the surface of PdZn alloys, and the correlation between surface structural/electronic properties and adsorption was found and discussed in detail. Five well-defined PdZn alloy surfaces, including PdZn p(2 × 1), β_1 -PdZn(111), "zigzag", β_1 -PdZn(010), and Zn-terminated β_1 -PdZn(001), were prepared by a CVD style technique using diethylzinc and palladium single crystals of Pd(111) and Pd(100). The characterization was performed by atomically resolved STM, LEED, HREELS, and XPS, and the experimental results were compared with DFT modeling.

Carbon monoxide served as a test molecule for palladium atomic configuration and for chemical properties of the alloys. Thus, HREELS showed that CO adsorbs only in the linear configuration on the β_1 -PdZn(010) surface, whereas only the bridge CO_{ads} was observed on Pd(100). The change of adsorption configuration from the bridge CO_{ads} to the linear CO_{ads} is due to the steric factor (geometric ensemble effect): the Pd–Pd distances in β_1 -PdZn(010) were 3.4 and 4.1 Å (the corresponding value for Pd(100) is 2.75 Å). Zn also destabilized CO adsorption on the PdZn p(2 \times 1) and β_1 -PdZn(111) structures (electronic ligand effect), which agrees with the DFT modeling results. The DFT prediction of the lower C-O stretching frequency observed on the PdZn alloy surfaces was consistent with the HREELS data, and it was explained by the electronic effect of Zn. The bridge and linear CO_{ads} have the same binding energy of -0.91 eV on the β_1 -PdZn(111) surface; therefore, both states were populated during the in situ HREELS experiment at RT. Because on the β_1 -PdZn(010) the binding energy difference is 0.26 eV, under similar conditions CO adsorbs in the linear configuration. DRIFTS spectra of CO adsorbed on PdZn nanoparticles supported on Al₂O₃ always showed both the linear and bridge CO stretching; the linear adsorption dominates at certain conditions. On the basis of our observations, this could be explained by adsorption of CO on the different planes of PdZn nanoparticles: β_1 -PdZn(010) accommodates the linear CO, and the linear and bridge CO adsorb on the β_1 -PdZn(111) plane.

Propylene was investigated as a product of propane dehydrogenation in the prospects of deeper dehydrogenation, hydrogenolysis, and coke formation. The experimental data and DFT modeling consistently showed the weakening of propylene adsorption on these PdZn alloy surfaces. The hydrocarbon fragments were detected only on the zigzag surface, where the aggregates of a few palladium atoms appeared. These observations could explain the high stability and selectivity of PdZn catalysts in propane dehydrogenation: disruption of propylene adsorption means a short resident time of the molecule on the catalytic surface, making further

dehydrogenation of propylene and hydrogenolysis hindered. We can hypothesize that the Pd-rich phase similar to the zigzag structure could be coked and be passivated during the PDH.

There are numerous studies of adsorption and reactions on bimetallic model surfaces, which greatly improve the understanding of the reaction mechanisms and driving forces. On the other hand, the interaction between Pd and Zn is rich: the phase diagram shows five major phases, and the β_1 phase has a wide range of Pd/Zn ratio from 27% to 44% of palladium. We have observed numerous surface structural transformation with slight variation of the Pd/Zn ratio triggered by varying of the annealing temperature. In this publication, we have focused on the most stable PdZn structure which we could reliably prepare. This allows us to make the link between structural and electronic properties of the PdZn alloys and the adsorption of CO and propylene.

ASSOCIATED CONTENT

Supporting Information

The Supporting Information is available free of charge at https://pubs.acs.org/doi/10.1021/acs.jpcc.2c01637.

Experimental details and parameters; C 1s XP spectra of PdZn near-surface alloys; STM and atomic arrangement of the PdZn zigzag structure (PDF)

AUTHOR INFORMATION

Corresponding Author

Dmitry Y. Zemlyanov — Birck Nanotechnology Center, Purdue University, West Lafayette, Indiana 47907, United States; Email: dimazemlyanov@purdue.edu

Authors

Cory A. Milligan – School of Chemical Engineering, Purdue University, West Lafayette, Indiana 47907, United States

Ranga Rohit Seemakurthi — School of Chemical Engineering, Purdue University, West Lafayette, Indiana 47907, United States

Junxian Gao – School of Chemical Engineering, Purdue University, West Lafayette, Indiana 47907, United States; orcid.org/0000-0002-1015-7103

Jeffrey P. Greeley — School of Chemical Engineering, Purdue University, West Lafayette, Indiana 47907, United States; orcid.org/0000-0001-8469-1715

Jeffrey T. Miller — School of Chemical Engineering, Purdue University, West Lafayette, Indiana 47907, United States; orcid.org/0000-0002-6269-0620

Fabio H. Ribeiro – School of Chemical Engineering, Purdue University, West Lafayette, Indiana 47907, United States

Complete contact information is available at: https://pubs.acs.org/10.1021/acs.jpcc.2c01637

Notes

The authors declare no competing financial interest.

■ ACKNOWLEDGMENTS

J.G., J.P.G., J.T.M., and D.Y.Z. gratefully acknowledge the financial support from the National Science Foundation under award no. 1804712. R.R.S, J.P.G., F.H.R., and J.T.M. were partially funded by the National Science Foundation under Cooperative Agreement No. EEC-1647722. C.A.M., F.H.R., and D.Y.Z. were partially funded by the United States Department of Energy (DOE) DE-FG02-03ER15408.

REFERENCES

- (1) Iwasa, N.; Kudo, S.; Takahashi, H.; Masuda, S.; Takezawa, N. Highly Selective Supported Pd Catalysts for Steam Reforming of Methanol. *Catal. Lett.* **1993**, *19*, 211–216.
- (2) Chin, Y.-H.; Dagle, R.; Hu, J.; Dohnalkova, A. C.; Wang, Y. Steam Reforming of Methanol over Highly Active Pd/Zno Catalyst. *Catalysis today* **2002**, *77*, 79–88.
- (3) Ranganathan, E. S.; Bej, S. K.; Thompson, L. T. Methanol Steam Reforming over Pd/Zno and Pd/Ceo2 Catalysts. *Appl. Catal. A: General* **2005**, 289, 153–162.
- (4) Iwasa, N.; Masuda, S.; Ogawa, N.; Takezawa, N. Steam Reforming of Methanol over Pd/Zno Effect of the Formation of Pdzn Alloys Upon the Reaction. *Appl. Catal.*, A 1995, 125, 145–157.
- (5) Föttinger, K.; van Bokhoven, J. A.; Nachtegaal, M.; Rupprechter, G. n. Dynamic Structure of a Working Methanol Steam Reforming Catalyst: In Situ Quick-Exafs on Pd/Zno Nanoparticles. *J. Phys. Chem. Lett.* **2011**, *2*, 428–433.
- (6) Rameshan, C.; et al. Subsurface-Controlled Co2 Selectivity of Pdzn near-Surface Alloys in H-2 Generation by Methanol Steam Reforming. *Angew. Chem., Int. Ed.* **2010**, 49, 3224–3227.
- (7) Rameshan, C.; et al. Steam Reforming of Methanol on Pdzn near-Surface Alloys on Pd(111) and Pd Foil Studied by in-Situ Xps. Leis and Pm-Iras. Journal of Catalysis 2010, 276, 101–113.
- (8) Bollmann, L.; Ratts, J. L.; Joshi, A. M.; Williams, W. D.; Pazmino, J.; Joshi, Y. V.; Miller, J. T.; Kropf, A. J.; Delgass, W. N.; Ribeiro, F. H. Effect of Zn Addition on the Water-Gas Shift Reaction over Supported Palladium Catalysts. *J. Catal.* **2008**, 257, 43–54.
- (9) Gallagher, J. R.; Childers, D. J.; Zhao, H. Y.; Winans, R. E.; Meyer, R. J.; Miller, J. T. Structural Evolution of an Intermetallic Pd-Zn Catalyst Selective for Propane Dehydrogenation. *Phys. Chem. Phys.* 2015, 17, 28144–28153.
- (10) Purdy, S. C.; Seemakurthi, R. R.; Mitchell, G. M.; Davidson, M.; Lauderback, B. A.; Deshpande, S.; Wu, Z.; Wegener, E. C.; Greeley, J.; Miller, J. T. Structural Trends in the Dehydrogenation Selectivity of Palladium Alloys. *Chem. Sci.* **2020**, *11*, 5066–5081.
- (11) Childers, D. J.; Schweitzer, N. M.; Shahari, S. M. K.; Rioux, R. M.; Miller, J. T.; Meyer, R. J. Modifying Structure-Sensitive Reactions by Addition of Zn to Pd. *J. Catal.* **2014**, *318*, 75–84.
- (12) Wu, Z.; Bukowski, B. C.; Li, Z.; Milligan, C.; Zhou, L.; Ma, T.; Wu, Y.; Ren, Y.; Ribeiro, F. H.; Delgass, W. N. Changes in Catalytic and Adsorptive Properties of 2 Nm Pt3mn Nanoparticles by Subsurface Atoms. *J. Am. Chem. Soc.* **2018**, *140*, 14870–14877.
- (13) LiBretto, N. J.; Yang, C.; Ren, Y.; Zhang, G.; Miller, J. T. Identification of Surface Structures in Pt3cr Intermetallic Nanocatalysts. *Chem. Mater.* **2019**, *31*, 1597–1609.
- (14) Chen, Z. X.; Neyman, K. M.; Gordienko, A. B.; Rosch, N. Surface Structure and Stability of Pdzn and Ptzn Alloys: Density-Functional Slab Model Studies. *Phys. Rev. B* **2003**, *68*, 8.
- (15) Bayer, A.; Flechtner, K.; Denecke, R.; Steinruck, H. P.; Neyman, K. M.; Rosch, N. Electronic Properties of Thin Zn Layers on Pd(111) During Growth and Alloying. *Surf. Sci.* **2006**, *600*, 78–94.
- (16) Chen, Z. X.; Neyman, K. M.; Lim, K. H.; Rosch, N. Ch3o Decomposition on Pdzn(111), Pd(111), and Cu(111). A Theoretical Study. *Langmuir* **2004**, *20*, 8068–8077.
- (17) Fasana, A.; Abbati, I.; Braicovich, L. Photoemission Evidence of Surface Segregation at Liquid-Nitrogen Temperature in Zn-Pd System. *Phys. Rev. B* **1982**, *26*, 4749–4751.
- (18) Rodriguez, J. A. Interactions in Bimetallic Bonding Electronic and Chemical-Properties of Pdzn Surfaces. *J. Phys. Chem.* **1994**, 98, 5758–5764.
- (19) Weirum, G.; Kratzer, M.; Koch, H. P.; Tamtogl, A.; Killmann, J.; Bako, I.; Winkler, A.; Surnev, S.; Netzer, F. P.; Schennach, R. Growth and Desorption Kinetics of Ultrathin Zn Layers on Pd(111). *J. Phys. Chem. C* **2009**, *113*, 9788–9796.
- (20) Koch, H. P.; Bako, I.; Weirum, G.; Kratzer, M.; Schennach, R. A Theoretical Study of Zn Adsorption and Desorption on a Pd(111) Substrate. *Surf. Sci.* **2010**, *604*, 926–931.

- (21) Jeroro, E.; Lebarbier, V.; Datye, A.; Wang, Y.; Vohs, J. M. Interaction of Co with Surface Pdzn Alloys. Surf. Sci. 2007, 601, 5546–5554.
- (22) Stadlmayr, W.; et al. Temperature-Induced Modifications of Pdzn Layers on Pd(111). J. Phys. Chem. C 2010, 114, 10850-10856.
- (23) Ruff, M.; Frey, S.; Gleich, B.; Behm, R. J. Au-Step Atoms as Active Sites for Co Adsorption on an and Bimetallic Au/Pd(111) Surfaces. *Appl. Phys. a-Mater.* **1998**, *66*, S513–S517.
- (24) Wendt, S.; Ozensoy, E.; Wei, T.; Frerichs, M.; Cai, Y.; Chen, M. S.; Goodman, D. W. Electronic and Vibrational Properties of Ultrathin Sio2 Films Grown on Mo(112). *Phys. Rev. B* **2005**, 72, 115409.
- (25) Wei, T.; Wang, J.; Goodman, D. W. Characterization and Chemical Properties of Pd-Au Alloy Surfaces. *J. Phys. Chem. C* **2007**, 111, 8781–8788.
- (26) Li, Z. J.; Gao, F.; Wang, Y. L.; Calaza, F.; Burkholder, L.; Tysoe, W. T. Formation and Characterization of Au/Pd Surface Alloys on Pd(111). Surf. Sci. 2007, 601, 1898–1908.
- (27) Ruff, M.; Takehiro, N.; Liu, P.; Norskov, J. K.; Behm, R. J. Size-Specific Chemistry on Bimetallic Surfaces: A Combined Experimental and Theoretical Study. *ChemPhysChem* **2007**, *8*, 2068–2071.
- (28) Eyrich, M.; Diemant, T.; Hartmann, H.; Bansmann, J.; Behm, R. J. Interaction of Co with Structurally Well-Defined Monolayer Ptau/Pt(111) Surface Alloys. *J. Phys. Chem. C* **2012**, *116*, 11154–11165.
- (29) Ma, Y.; Bansmann, J.; Diemant, T.; Behm, R. J. Formation, Stability and Co Adsorption Properties of Pdag/Pd(111) Surface Alloys. *Surf. Sci.* **2009**, *603*, 1046–1054.
- (30) Farkas, A. P.; Diemant, T.; Bansmann, J.; Behm, R. J. The Adsorption of Oxygen and Coadsorption of Co and Oxygen on Structurally Well-Defined Pdag Surface Alloys. *ChemPhysChem* **2012**, 13, 3516–3525.
- (31) Gao, J. X.; Sawant, K. J.; Miller, J. T.; Zeng, Z. H.; Zemlyanov, D.; Greeley, J. P. Structural and Chemical Transformations of Zinc Oxide Ultrathin Films on Pd(111) Surfaces. *Acs Appl. Mater. Inter* **2021**, *13*, 35113–35123.
- (32) Biedermann, L. B.; Bolen, M. L.; Capano, M. A.; Zemlyanov, D.; Reifenberger, R. G. Insights into Few-Layer Epitaxial Graphene Growth on 4h-Sic(000(1)over-Bar Substrates from Stm Studies. *Phys. Rev. B* **2009**, 79, 125411.
- (33) Smith, K. C.; Saenz, D. A.; Zemlyanov, D.; Voevodin, A. A. XPS Thickness Solver, September 2014 ed.; nanohub.org: https://nanohub.org/resources/xpsts, 2012.
- (34) Gharachorlou, A.; Detwiler, M. D.; Nartova, A. V.; Lei, Y.; Lu, J. L.; Elam, J. W.; Delgass, W. N.; Ribeiro, F. H.; Zemlyanov, D. Y. Palladium Nanoparticle Formation on Tio2(110) by Thermal Decomposition of Palladium(Ii) Hexafluoroacetylacetonate. *Acs Appl. Mater. Inter* **2014**, *6*, 14702–14711.
- (35) Zemlyanov, D. Y; Jespersen, M.; Zakharov, D. N; Hu, J.; Paul, R.; Kumar, A.; Pacley, S.; Glavin, N.; Saenz, D.; Smith, K. C; Fisher, T. S; Voevodin, A. A; et al. Versatile Technique for Assessing Thickness of 2d Layered Materials by Xps. *Nanotechnology* **2018**, *29*, 115705.
- (36) Fadley, C. S. Basic Concepts of X-Ray Photoelectron Spectroscopy. In *Electron Spectroscopy Theory, Techniques, and Applications*; Brundle, C. R., Baker, A. D., Eds.; Academic Press: New York, 1978; Vol. 2, pp 1–156
- (37) Powell, C. J.; Jablonski, A. NIST Electron Effective-Attenuation-Length Database; NIST: Gaitherburg, MD, 2011.
- (38) Horcas, I.; Fernandez, R.; Gomez-Rodriguez, J. M.; Colchero, J.; Gomez-Herrero, J.; Baro, A. M. Wsxm: A Software for Scanning Probe Microscopy and a Tool for Nanotechnology. *Rev. Sci. Instrum.* **2007**, *78*, 013705.
- (39) Seemakurthi, R. R.; Canning, G.; Wu, Z. W.; Miller, J. T.; Datye, A. K.; Greeley, J. Identification of a Selectivity Descriptor for Propane Dehydrogenation through Density Functional and Microkinetic Analysis on Pure Pd and Pd Alloys. ACS Catal. 2021, 11, 9588–9604.

- (40) Evans, S. Energy Calibration Secondary Standards for X-Ray Photoelectron Spectrometers. *Surface and interface analysis* **1985**, *7*, 299–302.
- (41) Gabasch, H.; Knop-Gericke, A.; Schlogl, R.; Penner, S.; Jenewein, B.; Hayek, K.; Klotzer, B. Zn Adsorption on Pd(111): Zno and Pdzn Alloy Formation. *J. Phys. Chem. B* **2006**, *110*, 11391–11398.
- (42) MacLeod, J. M.; Lipton-Duffin, J. A.; Baraldi, A.; Rosei, R.; Rosei, F. Surface Structure of Pd(111) with Less Than Half a Monolayer of Zn. *Phys. Chem. Chem. Phys.* **2013**, *15*, 12488–12494.
- (43) Stadlmayr, W.; Penner, S.; Klotzer, B.; Memmel, N. Growth, Thermal Stability and Structure of Ultrathin Zn-Layers on Pd(111). SURFACE SCIENCE 2009, 603, 251–255.
- (44) Kuhn, W. K.; Szanyi, J.; Goodman, D. W. Co Adsorption on Pd(111) the Effects of Temperature and Pressure. *Surf. Sci.* **1992**, 274, L611–L618.
- (45) Hoffmann, F. M. Infrared Reflection-Absorption Spectroscopy of Adsorbed Molecules. *Surf. Sci. Rep* **1983**, *3*, 107–192.
- (46) Bradshaw, A. M.; Hoffmann, F. M. Chemisorption of Carbon-Monoxide on Palladium Single-Crystal Surfaces Ir Spectroscopic Evidence for Localized Site Adsorption. Surf. Sci. 1978, 72, 513–535.
- (47) Crossley, A.; King, D. A. Infrared Spectra for Co Isotopes Chemisorbed on Pt "111": Evidence for Strong Absorbate Coupling Interactions. *Surf. Sci.* **1977**, *68*, 528–538.
- (48) Föttinger, K.; Rupprechter, G. n. In Situ Spectroscopy of Complex Surface Reactions on Supported Pd–Zn, Pd–Ga, and Pd (Pt)–Cu Nanoparticles. *Accounts of chemical research* **2014**, 47, 3071–3079.
- (49) Tamtogl, A.; Kratzer, M.; Killman, J.; Winkler, A. Adsorption/Desorption of H-2 and Co on Zn-Modified Pd(111). *J. Chem. Phys.* **2008**, *129*, 224706.
- (50) Smirnov, M. Y.; Gorodetskii, V. V.; Cholach, A. R.; Zemlyanov, D. Y. Hydrogenation of Isolated Atoms and Small Clusters of Carbon on Pt(111) Surface Hreels Tds Studies. *Surf. Sci.* **1994**, *311*, 308–321.
- (51) Guo, X. C.; Madix, R. J. Origin of Vinylic C-H Bond Activation in the Combustion of Alkenes on Palladium: An Hreels Study of Propene on $Pd(100)-P(2 \times 2)-O$. Surf. Sci. 1997, 391, L1165–L1171.
- (52) Massalski, T. B.; Okamoto, H.; Subramanian, P. R.; Kacprzak, L. *Binary Alloy Phase Diagrams*; ASM International: Materials Park, OH, 1990.

☐ Recommended by ACS

Novel Insights on the Metal–Support Interactions of Pd/ZrO_2 Catalysts on CH_4 Oxidation

Qi Li, Junhua Li, et al.

FEBRUARY 06, 2023

ACS APPLIED MATERIALS & INTERFACES

READ 🗹

Bismuth-Modulated Surface Structural Evolution of Pd₃Bi Intermetallic Alloy Catalysts for Selective Propane Dehydrogenation and Acetylene Semihydrogenation

Wenqing Zhang, Jeffrey T. Miller, et al.

AUGUST 11, 2022

ACS CATALYSIS

READ 🗹

Insights into Palladium Deactivation during Advanced Oxidation Processes

Verónica Pinos-Vélez, Anton Dafinov, et al.

SEPTEMBER 28, 2022

CHEMISTRY OF MATERIALS

READ 🗹

Antisintering Pd₁ Catalyst for Propane Direct Dehydrogenation with In Situ Active Sites Regeneration Ability

Mi Peng, Ding Ma, et al.

JANUARY 31, 2022

ACS CATALYSIS

READ 🗹

Get More Suggestions >